Experimental and numerical study of pressure drop and heat transfer in a single-phase micro-channel heat sink

Weilin Qu, Issam Mudawar [*]

Boiling and Two-phase Flow Laboratory, School of Mechanical Engineering, 1288 Mechanical Engineering Building, Purdue University, West Lafayette, IN 47907-1288, USA

Abstract

The pressure drop and heat transfer characteristics of a single-phase micro-channel heat sink were investigated both experimentally and numerically. The heat sink was fabricated from oxygen-free copper and fitted with a polycarbonate plastic cover plate. The heat sink consisted of an array of rectangular micro-channels 231 μm wide and 713 μm deep. Deionized water was employed as the cooling liquid and two heat flux levels, $q''_{eff} = 100$ W/cm^2 and $q''_{eff} = 200$ W/cm^2, defined relative to the planform area of the heat sink, were tested. The Reynolds number ranged from 139 to 1672 for $q''_{eff} = 100$ W /cm^2, and 385 to 1289 for $q''_{eff} = 200$ W /cm^2. The three-dimensional heat transfer characteristics of the heat sink were analyzed numerically by solving the conjugate heat transfer problem involving simultaneous determination of the temperature field in both the solid and liquid regions. Also presented and discussed is a detailed description of the local and average heat transfer characteristics of the heat sink. The measured pressure drop and temperature distributions show good agreement with the corresponding numerical predictions. These findings demonstrate that the conventional Navier–Stokes and energy equations can adequately predict the fluid flow and heat transfer characteristics of micro-channel heat sinks. © 2002 Elsevier Science Ltd. All rights reserved.

1. Introduction

Micro-channel heat sinks constitute an innovative cooling technology for the removal of a large amount of heat from a small area. The heat sink is usually made from a high thermal conductivity solid such as silicon or copper with the micro-channels fabricated into its surface by either precision machining or micro-fabrication technology. These micro-channels have characteristic dimensions ranging from 10 to 1000 μm, and serve as flow passages for the cooling liquid. Micro-channel heat sinks combine the attributes of very high surface area to volume ratio, large convective heat transfer coefficient, small mass and volume, and small coolant inventory. These attributes render these heat sinks very suitable for cooling such devices as high-performance microprocessors, laser diode arrays, radars, and high-energy-laser mirrors.

The micro-channel heat sink cooling concept was first introduced by Tuckerman and Pease in the early 1980s [1]. They fabricated a rectangular micro-channel heat sink in a 1×1 cm^2 silicon wafer. The channels had a width of 50 μm and a depth of 302 μm, and were separated by 50 μm thick walls. Using water as cooling fluid, the micro-channel heat sink was capable of dissipating 790 W/cm^2 with a maximum substrate temperature raise of 71 °C above the water inlet temperature and a pressure drop of 2.2 bar (31 psi).

Due to their inherent advantages, micro-channel heat sinks have received considerable attention since Tuckerman and Pease's pioneering study. Several studies have since been published which can be grouped as analytical [2–8], numerical [9,10], or experimental [11–20].

The primary objective of most of the analytical studies is to develop design schemes which can be used to optimize the dimensions of the heat sink. This is typically accomplished by minimizing the overall thermal resistance of the heat sink for a given pressure drop.

---

[*] Corresponding author. Tel.: +1-765-494-5705; fax: +1-765-494-0539.

E-mail address: mudawar@ecn.purdue.edu (I. Mudawar).

Nomenclature

A_{bot}	area of unit cell bottom wall occupied by copper
A_c	cross-sectional area of channel
A_t	area of overall heat sink top surface
c_p	specific heat at constant pressure
d_h	hydraulic diameter of channel, four times ratio of cross-sectional area to wetted perimeter
h_{conv}	natural convection heat transfer coefficient
H	height of unit cell
H_{ch}	height of channel
H_{w1}	thickness of cover plate
H_{w2}	thickness from unit cell bottom wall to channel bottom wall
i	number of iteration
k	thermal conductivity
K_{c1}, K_{c2}	contraction loss coefficient
K_{e1}, K_{e2}	expansion loss coefficient
L	length of unit cell
L_1, L_2, L_3, L_4	distance between thermocouple holes
n	outer normal coordinate at interface between solid and liquid
N	number of channels in heat sink
Nu	Nusselt number
P	pressure
P_w	power supplied to micro-channel heat sink
ΔP	total pressure drop
ΔP_{ch}	pressure drop along micro-channels
$\Delta P_{c1}, \Delta P_{c2}$	contraction pressure loss
$\Delta P_{e1}, \Delta P_{e2}$	expansion pressure loss
q''	heat flux
q''_{bot}	heat flux at unit cell bottom wall occupied by copper
q''_{eff}	effective heat flux based on planform area of heat sink top surface
Re	Reynolds number
T	temperature
T_{in}	fluid inlet temperature
T_m	fluid bulk temperature
T_∞	ambient temperature
u	velocity component in x direction
u_{in}	fluid inlet velocity
u_{out}	fluid outlet velocity
v	velocity component in y direction
$\vec{V}$	velocity vector
$\dot{V}$	volume flow rate
w	velocity component in z direction
W	width of unit cell
W_{ch}	width of channel
W_w	half-width of wall separating channels
x	Cartesian coordinate
y	Cartesian coordinate
z	Cartesian coordinate

Greek symbols

μ	dynamic viscosity
ρ	density

Subscripts

av	average
f	fluid
in	inlet
out	outlet
p1	deep plenum
p2	shallow plenum
s	solid
Γ	interface between solid and liquid

Among others, Knight et al. [5,6] presented an optimization scheme that included both laminar and turbulent flow. Their results indicated that when the pressure drop is small, laminar flow prevails, yielding low thermal resistance. Conversely, when the pressure drop is large, the optimal thermal resistance is found in the turbulent region.

To develop such an optimization design scheme, it is essential to have an analytical description of the transport processes in the heat sink. Heat transfer in the micro-channel is a conjugate one, combining heat conduction in the solid and convection to the cooling fluid. Due to the complicated nature of this flow, it is impossible to develop a comprehensive analytical solution for the governing differential equations. Therefore, most analytical studies adopt the classical fin analysis method, which models the solid walls separating micro-channels as thin fins, and simplifies the heat transfer process by introducing such major approximations as one-dimensional heat transfer, constant convective heat transfer coefficient, and uniform fluid temperature. While the classical fin analysis method provides a simple method to describing the heat transfer performance of a micro-channel heat sink, its accuracy can be greatly compromised by its simplifying assumptions.

A more accurate description of the fluid flow and heat transfer characteristics of a micro-channel heat sink necessitates the use of direct numerical simulation methods. Wesberg et al. [9] performed a two-dimensional numerical analysis by assuming both hydraulically and thermally fully developed flow within the micro-channels. Fedorov and Viskanta [10] developed a three-dimensional model by eliminating the approximation of fully developed flow, accounting for devel-

opment of both the velocity and temperature fields. No detailed comparison between the experimental results and numerical predictions was provided in these studies to validate the numerical analysis.

In addition to the above-mentioned analytical and numerical studies, several experimental studies can be found in the literature. Micro-channel heat sinks with different materials, dimensions, and cooling fluids were fabricated and tested. An excellent review of the experimental studies in the 1980s was provided by Phillips [4]. More recent experimental investigations were conducted by Ravigururajan et al. [16], Harms et al. [17,19], Rahman and Gui [14,15], Rahman [20], and Kawamo et al. [18]. Ravigururajan et al. [16] tested a copper micro-channel heat sink with 270 μm wide and 1000 μm deep micro-channels. The overall heat sink was 2.25 cm long and 2.42 cm wide. Results for Refrigerant-124 showed the heat transfer coefficient increased between 300% and 900% compared with the theoretical value for laminar flow based on a Nusselt number of 4.36. They attributed this enhancement to thinning of the boundary layer in the narrow channels. Rahman and Gui [14] tested three micro-channel heat sinks fabricated in silicon wafers. The micro-channels were 1.0 mm wide and 221, 254, 278 μm in depth, and the overall heat sink was 4.8 cm long and 4.6 cm wide. Measured values of the average Nusselt number for water were larger than predicted analytically for developing laminar flow. This enhancement was attributed to breakage of the velocity boundary layer by micro-surface roughness. The transition from laminar to turbulent flow was somewhat gradual because the small channel dimension was of the same order of magnitude as the length scale of turbulent eddies. Harms et al. [17] tested a 2.5 cm long, 2.5 cm wide silicon heat sink having 251 μm wide and 1030 μm deep micro-channels. A relatively low Reynolds number

of 1500 marked transition from laminar to turbulent flow, which was attributed to a sharp inlet, relatively long entrance region, and channel surface roughness. They concluded the classical relation for local Nusselt number was fairly accurate for modeling micro-channel flows.

Although many studies have been conducted on micro-channel heat sinks, findings remain inconclusive, especially when comparing experimental results with theoretical predictions. It is evident that an effective design of micro-channel heat sinks requires a fundamental understanding of the fluid flow and heat transfer characteristics in micro-channels. Detailed experimental measurements and theoretical predictions of the local and average heat sink temperature, heat flux, and Nusselt number are essential to acquiring this fundamental understanding.

In this study, the pressure drop and heat transfer characteristics of a single-phase micro-channel heat sink are investigated both experimentally and numerically. The experimental results are compared with the numerical predictions to assess the suitability of macro transport models in depicting the transport characteristics of micro-channel heat sinks. A detailed description of the local and average heat transfer characteristics is presented and discussed. These results provide new, fundamental insight into the complex three-dimensional characteristics of these heat sink.

2. Experimental apparatus

2.1. Flow loop

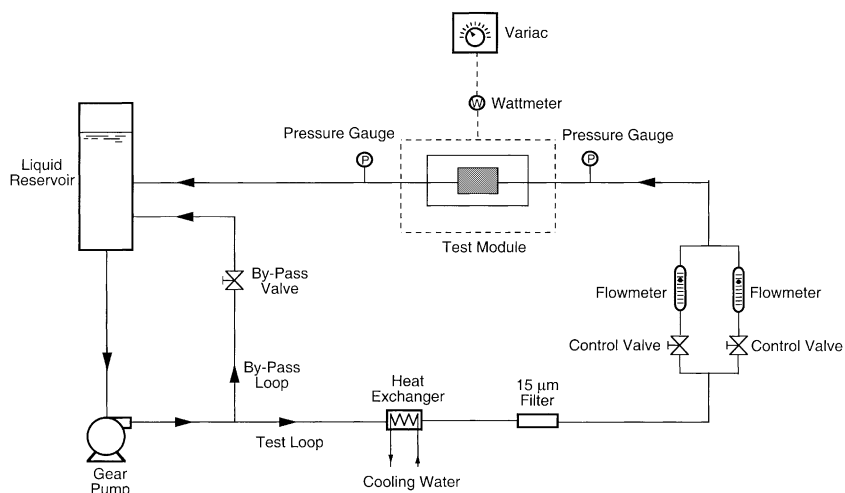Fig. 1 shows the flow loop that was constructed to supply deionized water to the heat sink at the desired

Fig. 1. Schematic of flow loop.

pressure, temperature, and flow rate. The water was pumped from a liquid reservoir and circulated through the flow loop by a gear pump. Upon exiting the pump, a portion of the flow, controlled by a by-pass valve, entered the test loop containing the heat sink, while the remaining portion returned to the reservoir though a by-pass loop. The test loop water first passed through a heat exchanger where the water was cooled to the desired inlet temperature. The water then passed through a 15 μm filter to prevent any solid particles from blocking the heat sink micro-channels. After exiting the filter, the water was routed to one of two rotameters for volume flow rate measurement. The water then entered the micro-channel heat sink test module where the electric power supplied to the heat sink was removed by the water. Leaving the test module, the water returned to the reservoir where it mixed with the by-passed flow.

2.2. Test module

The test module consisted of a micro-channel heat sink, housing, cover plate, and 12 cartridge heaters as illustrated in Fig. 2(a). A schematic of the micro-channel heat sink with key dimensions is shown in Fig. 2(b). The micro-channel heat sink was fabricated from a single block of oxygen-free copper. The planform (top) surface of the heat sink measured 1.0 cm wide and 4.48 cm long. Twenty-one rectangular micro-slots were machined into the heat sink top surface by a precision sawing technique. The micro-slots were equidistantly spaced within the 1-cm heat sink width and had the cross-sectional dimensions of 231 μm wide and 712 μm deep. Below the heat sink top surface were four 0.36 mm diameter holes which were drilled into the side wall of the heat sink up to the center plane. Four Chromel–Alumel (Type-K) thermocouples with a 0.33 mm bead diameter were inserted into these holes to measure the temperature distribution inside the heat sink. Below the thermocouple holes, a small protruding platform was machined around the periphery of the heat sink to both facilitate accurate positioning of the heat sink in the housing and ensure adequate surface area for sealing. This platform effectively divided the heat sink into an upper portion and a lower portion that will be discussed later in conjunction with the heat sink's numerical model. Twelve 6.35 mm diameter holes were drilled into the lower portion of the heat sink to accommodate the cartridge heaters. These cartridge heaters were connected in parallel and powered by a single 0-110 VAC variac. Power dissipation by the cartridge heaters was measured by a wattmeter. As shown in Fig. 2(b), three 1.6 mm slots
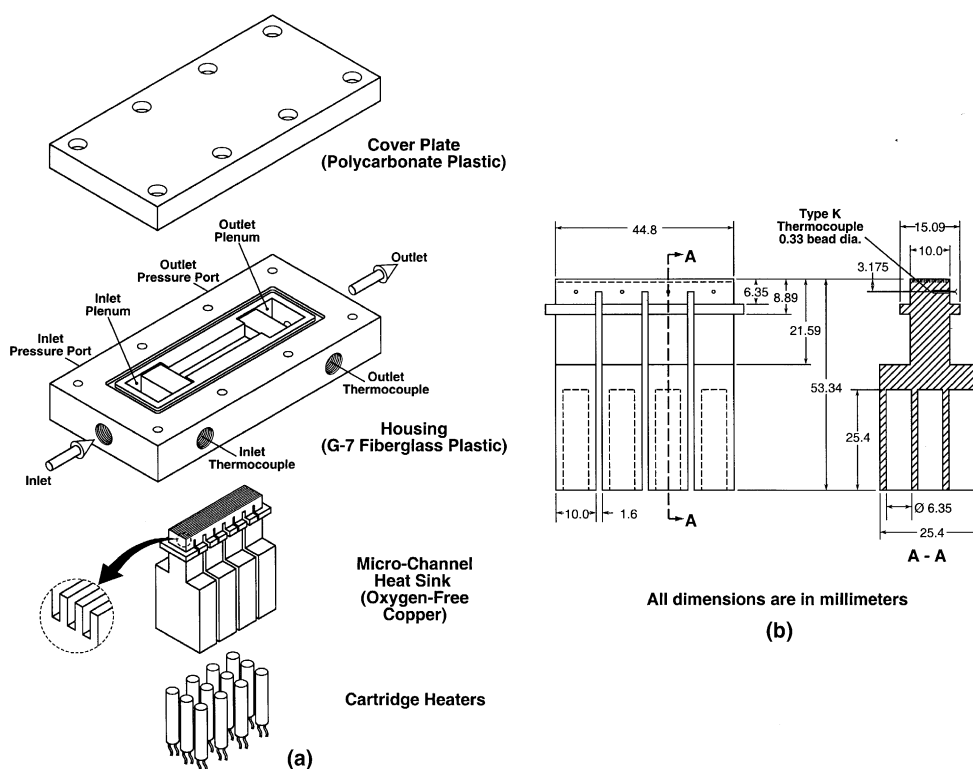

Fig. 2. (a) Test module. (b) Micro-channel heat sink.

were cut from the bottom surface up through most of the heat sink's height including part of the upper portion. These slots aided in reducing heat spread within the lower portion of the heat sink and providing a more uniform heat flux distribution.

The heat sink housing was made from G-7 fiberglass plastic. The central part of the housing was removed where the heat sink was inserted as illustrated in Fig. 2(a). The protruding portion of the heat sink ensured the top surface of the heat sink was flush with the top surface of the housing. RTV silicone rubber was applied along the interface between the housing and the heat sink to prevent leakage. The housing contained plenums both upstream and downstream of the micro-channels. Each plenum had a deep portion leading to a shallow portion to help ensure even distribution of the flow between micro-channels as well as even exit mixing. Two absolute pressure transducers were connected to the deep portions of inlet and outlet plenums via pressure taps to measure the inlet and exit pressures, respectively. Also located in the inlet and outlet plenums were two Type-K thermocouples to measure the inlet and exit temperatures of the water, respectively.

A cover plate made from polycarbonate plastic (Lexan) was bolted atop the housing to hold the heat sink securely in place. The cover plate and micro-slots in the heat sink top surface formed closed micro-channels. An O-ring in the housing maintained a leak-proof seal.

2.3. Data acquisition

During tests, the power dissipated by the cartridge heaters was adjusted manually by the variac. Two input power levels were tested. They were defined by an effective heat flux q''_{eff}, based on the top planform area of the heat sink, $A_t = 1.0 \times 4.48$ cm^2:

$$q''_{eff} = \frac{P_W}{A_t},\tag{1}$$

where P_W is the total electric power input measured using the wattmeter. The two heat flux levels tested were $q''_{eff} = 100$ W/cm^2 and $q''_{eff} = 200$ W/cm^2. The pump and by-pass valve were set to produce a constant water flow rate during a given test. A broad range of flow rates was examined, from 93.5 to 1136.4 ml/min for $q''_{eff} = 100$ W/cm^2, and 259.1 to 859.5 ml/min for $q''_{eff} = 200$ W/cm^2. These flow rates correspond to Reynolds numbers from 139 to 1672 for $q''_{eff} = 100$ W/cm^2 and 385 to 1289 for $q''_{eff} = 200$ W/cm^2, where the Reynolds number is based on inlet parameters:

$$Re = \frac{\rho_f u_{in} d_h}{\mu_{f,in}},\tag{2}$$

u_{in} is the inlet velocity:

$$u_{in} = \frac{\dot{V}}{N A_{ch}},\tag{3}$$

and $\mu_{f,in}$ is evaluated using the measured inlet temperature. Using the heat exchanger located in the flow loop, the water inlet temperature was set to 15 °C. Once desired experimental conditions were reached, the heat sink was allowed to reach steady-state conditions, typically within 30–60 min. Once at steady state, three sets of readings from the rotameters, the thermocouples, pressure transducers, and wattmeter were recorded at 15 min intervals.

2.4. Measurement uncertainty

Heat loss to the ambient was estimated at less than 1% of the total heat input. Therefore, heat losses were assumed negligible, and cartridge heater power measured by the wattmeter was used for all heat flux calculations. Excellent agreement between electrical power input and measured enthalpy change of the cooling water further verified this assumption. This issue will be addressed in more details later in this paper. Measurement uncertainties associated with the wattmeter, rotameters, and pressure transducers were less than 0.5%, 4% and 3.5%, respectively. Error associated with the thermocouple measurements was estimated at less than 0.3 °C.

3. Results and discussion

In this section, the three-dimensional fluid flow and heat transfer characteristics of the heat sink are first analyzed numerically. Then, the measured performance presented and compared with the numerical predictions. Finally, detailed descriptions of the local and average heat transfer characteristics of the heat sink are discussed based on the numerical results.

3.1. Numerical analysis

A unit cell containing a single micro-channel and surrounding solid is chosen to perform the numerical analysis. Symmetry allows these results to be easily extended to the entire heat sink. Fig. 3 illustrates the unit cell and corresponding coordinate system and key notations. Dimensions of the unit cell are given in Table 1.

An alternative unit cell configuration which was not used in the present study is one utilizing the channel mid-plane ($0 \leqslant x \leqslant L$, $y = W/2$, and $0 \leqslant z \leqslant H$) as the unit cell boundary. This arrangement is computationally more efficient since fewer nodes are needed. However, because the velocity and temperature gradients within the flow channel are much larger than those in the surrounding solid, a large numerical error may be incurred
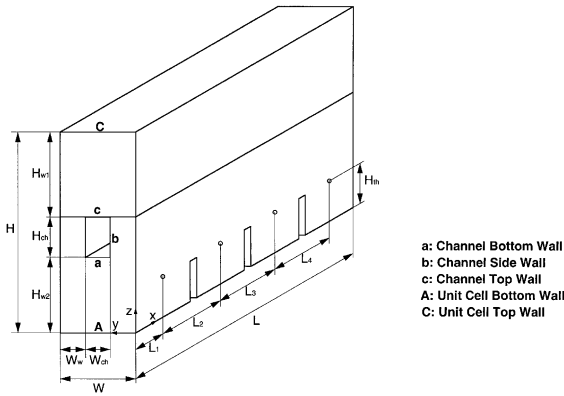
Fig. 3. Schematic of heat sink unit cell for numerical simulation.

when discretizing the channel mid-plane boundary. This may compromise the accuracy of the numerical scheme.

Heat transfer in the unit cell is a conjugate one combining heat conduction in the solid and convection to the cooling fluid. The two heat transfer modes are coupled by continuities of temperature and heat flux at the interface between the solid and fluid, which are expressed as

$$T_{s,\Gamma} = T_{f,\Gamma}, \tag{4}$$

$$-k_s \frac{\partial T_s}{\partial n}\bigg|_{\Gamma} = -k_f \frac{\partial T_f}{\partial n}\bigg|_{\Gamma}. \tag{5}$$

Several simplifying assumptions are incorporated before establishing governing equations for the fluid flow and heat transfer in the unit cell:

(1) steady fluid flow and heat transfer;
(2) incompressible fluid;
(3) laminar flow;
(4) negligible radiation heat transfer;
(5) constant solid and fluid properties except water viscosity;
(6) negligible natural convection of air trapped in the deep slots of the heat sink.

Further explanations are needed for assumption (5) and (6). In assumption (5), the solid and liquid properties are assumed constant because variations of these properties are small within the temperature range tested. However, the variation of water viscosity is significant.

Therefore, variable temperature-dependent water viscosity based on mean temperature is employed. Natural convection of air within the deep slots is neglected (assumption (6)) because the small, deep slots suppress natural circulation within the slots. Therefore, the plastic cover plate, copper block and air within the deep slots are treated as a unitary "solid" region with a different thermal conductivity value assigned to each region. In the following section, subscript s is used to denote these "solid" regions.

Based on the above assumptions, the governing differential equations used to describe the fluid flow and heat transfer in the unit cell are expressed as follows. For the cooling water, the continuity, momentum, and energy equations are expressed, respectively, as

$$\nabla \vec{V} = 0, \tag{6}$$

$$\rho_f \left(\vec{V} \cdot \nabla \vec{V} \right) = -\nabla P + \nabla \cdot \left(\mu_f \nabla \vec{V} \right), \tag{7}$$

$$\rho_f c_{p,f} \left(\vec{V} \cdot \nabla T \right) = k_f \nabla^2 T. \tag{8}$$

For the solid regions, the continuity and momentum equations are simply

$$\vec{V} = 0, \tag{9}$$

and the energy equation is

$$k_s \nabla^2 T = 0. \tag{10}$$

A numerical method to solve this conjugate heat transfer problem is to treat the solid and fluid as a unitary computational domain and solve the above governing equations simultaneously [21,22]. Using this method, which is described later, only boundary conditions for the unit cell are needed, which are specified as follows.

First, consider the hydraulic boundary conditions. A uniform velocity is applied at the channel inlet:

$$u = u_{in}, \quad v = 0, \quad w = 0 \quad \text{for } x = 0,$$
$$W_w \leqslant y \leqslant W_w + W_{ch} \text{ and } H_{w2} \leqslant z \leqslant H_{w2} + H_{ch}. \tag{11}$$

The flow is assumed fully developed at the channel outlet:

$$\frac{\partial u}{\partial x} = 0, \quad \frac{\partial v}{\partial x} = 0, \quad \frac{\partial w}{\partial x} = 0 \quad \text{for } x = L,$$
$$W_w \leqslant y \leqslant W_w + W_{ch} \text{ and } H_{w2} \leqslant z \leqslant H_{w2} + H_{ch}. \tag{12}$$

Table 1
Dimensions of micro-channel heat sink unit cell

W_w (μm)	W_{ch} (μm)	H_{w1} (μm)	H_{ch} (μm)	H_{w2} (μm)	H_{th} (μm)
118	231	12 700	713	5637	3175
L_1 (mm)	L_2 (mm)	L_3 (mm)	L_4 (mm)	L (mm)	
5	11.588	11.588	11.588	44.764	

The velocity is zero along all other solid boundaries.

Thermal boundary conditions are given as follows. For the solid region, a constant heat flux is applied at the unit cell bottom, copper wall (Wall A):

$$-k_s \frac{\partial T}{\partial z} = q''_{bot} \quad \text{for } 0 \leqslant x \leqslant L, \ 0 \leqslant y \leqslant W \text{ and } z = 0,$$

$$(13)$$

where q''_{bot} is calculated from

$$q''_{bot} = \frac{P_W}{NA_{bot}}.$$

$$(14)$$

At the unit cell top wall (Wall C), natural convection is assumed:

$$-k_s \frac{\partial T}{\partial z} = h_{conv}(T - T_\infty)$$
$$\text{for } 0 \leqslant x \leqslant L, \ 0 \leqslant y \leqslant W \text{ and } z = H,$$

$$(15)$$

where h_{conv} is the convective heat transfer coefficient which is estimated at 10 W/°C m^2. T_∞ is the ambient temperature of 25 °C. Adiabatic boundary conditions are applied to all other boundaries of the solid region.

The inlet temperature of the cooling water is set equal to the water temperature measured at the channel inlet:

$$T = T_{in} \quad \text{for } x = 0, \ W_w \leqslant y \leqslant W_w + W_{ch}$$
$$\text{and } H_{w2} \leqslant z \leqslant H_{w2} + H_{ch}.$$

$$(16)$$

The flow is assumed thermally fully developed at the channel outlet:

$$\frac{\partial^2 T}{\partial x^2} = 0 \quad \text{for } x = L, \ W_w \leqslant y \leqslant W_w + W_{ch}$$
$$\text{and } H_{w2} \leqslant z \leqslant H_{w2} + H_{ch}.$$

$$(17)$$

It should be noted here that the temperature field might not be fully developed if the thermal entrance length is longer than the channel itself. However, the change of temperature gradient along the flow direction at the channel exit is quite small even for very large Reynolds numbers. Therefore, using Eq. (17) as an exit thermal boundary condition will not influence the accuracy of the numerical results.

As mentioned before, the entire unit cell can be treated as a unitary computational domain. The governing differential equations, Eqs. (6)–(10), together with the boundary conditions, are discretized along the three spatial coordinates using the finite difference method, which results in a system of algebraic equations. The SIMPLE algorithm [21] is then applied to solve the resulting system of equations in primitive variables, namely u, v, w, P, and T. Appropriate values are assigned for the thermophysical properties in the solid and fluid regions. When solving the momentum equations, a very large value is assigned to the viscosity in the solid. Since velocity at all the liquid–solid boundaries is specified as zero, a very large solid viscosity will result in zero velocity throughout the solid. The Gauss–Seidal iterative technique is employed during the solution process, with successive over-relaxation to improve convergence time. The solution is regarded convergent when the criterion of $\max |(\phi^{i+1} - \phi^i)/\phi^{i+1}| \leqslant 10^{-6}$ is satisfied, where ϕ represents any dependent variable, namely u, v, w, or T, and i is the iteration number.

The grid system employed in the present numerical analysis has 102, 22, and 43 nodes in the x, y and z-directions, respectively. A non-uniform grid arrangement in the x-direction, with a larger number of grid points near the channel inlet, is used to resolve the developing region. In order to check the sensitivity of the numerical results to mesh size, three different grid systems were tested. They consisted of $62 \times 12 \times 23$, $102 \times 22 \times 43$, and $122 \times 42 \times 63$ nodes in the x, y, and z directions, respectively. The results from the last two grid systems were very close to each other and local temperature differences were less than 0.1%. Since less computational time and computer memory were needed for the second grid system, it was employed in the final simulation.

3.2. Experimental results and comparison with numerical predictions

Fig. 4(a) shows the measured pressure drop increasing with increasing Reynolds number. The largest
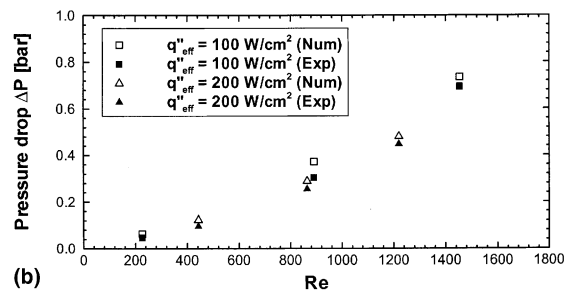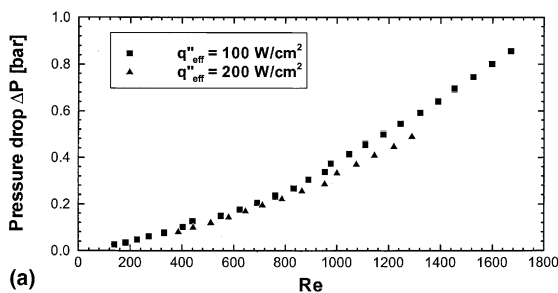

Fig. 4. (a) Variation of measured pressure drop with Reynolds number. (b) Comparison of measured and predicted values of pressure drop.

pressure drop of 0.86 bar was measured at $q''_{\mathrm{eff}} = 100$ W/cm^2 and $Re = 1672$. For the same Reynolds number, the pressure drop is lower for $q''_{\mathrm{eff}} = 200$ W/cm^2 because the higher water temperature at this condition decreases water viscosity.

A comparison between measured and predicted pressure drops for the two heat flux levels and different Reynolds numbers is shown in Fig. 4(b). The predicted pressure drop accounts for the pressure drop along the micro-channels, as well as the pressure losses associated with the abrupt contraction and expansion at the micro-channel inlet and outlet, respectively. A complete expression for the total pressure drop is

$$\Delta P = \Delta P_{\mathrm{c1}} + \Delta P_{\mathrm{c2}} + \Delta P_{\mathrm{ch}} + \Delta P_{\mathrm{e2}} + \Delta P_{\mathrm{e1}}, \qquad (18)$$

where the individual components are as follows. ΔP_{ch} is the pressure drop across the micro-channels, which can be obtained from the numerical simulation. ΔP_{c1} and ΔP_{c2} are the contraction pressure losses from the deep plenum to the shallow plenum, and from the shallow plenum to the micro-channels, respectively. They are expressed as [23]

$$\Delta P_{\mathrm{c1}} = \frac{1}{2}\rho_{\mathrm{f}}\left(u_{\mathrm{p2,in}}^2 - u_{\mathrm{p1,in}}^2\right) + \frac{K_{\mathrm{c1}}}{2}\rho_{\mathrm{f}}u_{\mathrm{p2,in}}^2, \qquad (19)$$

and

$$\Delta P_{\mathrm{c2}} = \frac{1}{2}\rho_{\mathrm{f}}\left(u_{\mathrm{in}}^2 - u_{\mathrm{p2,in}}^2\right) + \frac{K_{\mathrm{c2}}}{2}\rho_{\mathrm{f}}u_{\mathrm{in}}^2, \qquad (20)$$

where subscripts p1 and p2 denote the deep plenum and shallow plenum, respectively, and K_{c1} and K_{c2} are the loss coefficients for the abrupt contractions. Similarly, ΔP_{e2} and ΔP_{e2} are the expansion pressure losses from the micro-channels to the shallow plenum, and from the shallow plenum to the deep plenum, respectively, which are expressed as

$$\Delta P_{\mathrm{e2}} = \frac{1}{2}\rho_{\mathrm{f}}\left(u_{\mathrm{p2,out}}^2 - u_{\mathrm{out}}^2\right) + \frac{K_{\mathrm{e2}}}{2}\rho_{\mathrm{f}}u_{\mathrm{out}}^2, \qquad (21)$$

and

$$\Delta P_{\mathrm{e1}} = \frac{1}{2}\rho_{\mathrm{f}}\left(u_{\mathrm{p1,out}}^2 - u_{\mathrm{p2,out}}^2\right) + \frac{K_{\mathrm{e1}}}{2}\rho_{\mathrm{f}}u_{\mathrm{p2,out}}^2, \qquad (22)$$

where K_{e1} and K_{e2} are the loss coefficients associated with the abrupt expansion. For the present heat sink test module geometry, the values of K_{c1}, K_{c2}, K_{e1} and K_{e2} are close to unity.

Fig. 4(b) shows good agreement between the measured and predicted pressure drops. For a fluid with constant properties flowing through a rectangular channel, one would expect a linear relationship between pressure drop and Reynolds number. There are several reasons for the slope change in the pressure drop characteristics in Figs. 4(a) and (b). First, for constant power input and water inlet temperature, the
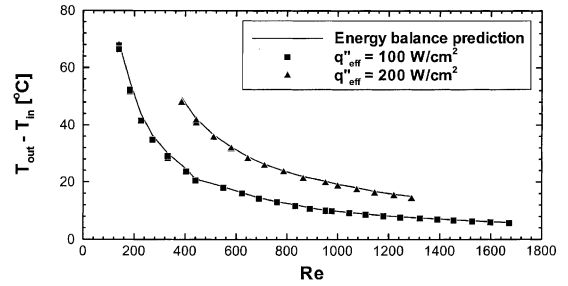

Fig. 5. Comparison of experimental data and energy balance predictions for water temperature rise from heat sink inlet to outlet: (a) $q''_{\mathrm{eff}} = 100$ W/cm^2, (b) $q''_{\mathrm{eff}} = 200$ W/cm^2.

outlet water temperature should decrease with increasing Reynolds number as shown in Fig. 5. This in turn increases water viscosity, resulting in a larger pressure drop. Second, the inlet and outlet pressure losses are proportional to the square of velocity as indicated in Eqs. (19)–(22). Therefore, increasing Reynolds number produces a more pronounced increase in the inlet and outlet pressure losses. Another interesting observation from the experimental pressure drop results is the absence of an early transition from laminar to turbulent flow within the Reynolds number range tested.

Fig. 5 compares the measured water temperature rise between the channel inlet and outlet, and theoretical values predicted from the simple energy balance

$$\rho_{\mathrm{f}}\dot{V}c_{\mathrm{p,f}}(T_{\mathrm{out}} - T_{\mathrm{in}}) = P_{\mathrm{W}}. \qquad (23)$$

The excellent agreement between the two proves virtually all the electrical power supplied by the cartridge heaters was removed by the water, and heat losses are indeed negligible.

Figs. 6(a) and (b) show readings from the four thermocouples located inside the heat sink for $q''_{\mathrm{eff}} = 100$ W/cm^2 and $q''_{\mathrm{eff}} = 200$ W/cm^2, respectively. The locations of the thermocouples are illustrated in Figs. 2(b) and 3. For each location, Figs. 6(a) and (b), show temperature decreases with increasing Reynolds number, which is similar to the water temperature rise data in Fig. 5. For the same Reynolds number, the temperature increases along the flow direction. Also for the same Reynolds number, the temperature for a given location is higher for $q''_{\mathrm{eff}} = 200$ W/cm^2 than for $q''_{\mathrm{eff}} = 100$ W/cm^2.

Figs. 7(a) and (b) compare the temperatures measured along the thermocouple line with numerical predictions for the two heat fluxes and different Reynolds numbers. As expected, the heat sink temperature increases along the flow direction. The shallow dips in the predicted distributions correspond to locations of the deep slots where air is trapped. The good agreement between the measured and predicted temperatures
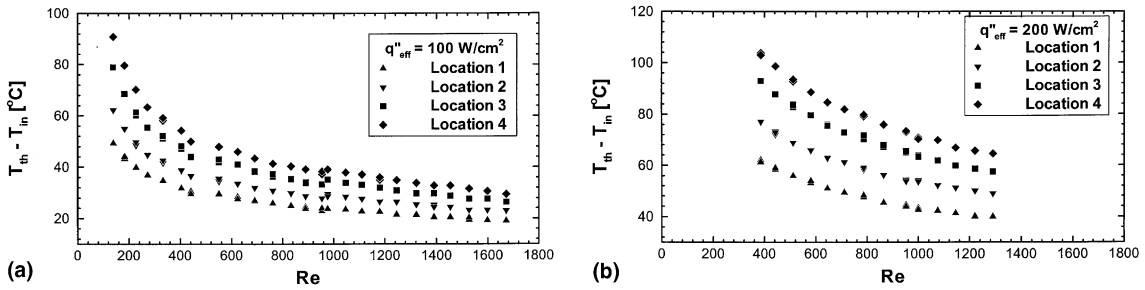
Fig. 6. Thermocouple readings inside micro-channel heat sink versus Reynolds number for (a) $q''_{eff} = 100$ W/cm^2 and (b) $q''_{eff} = 200$ W/cm^2.
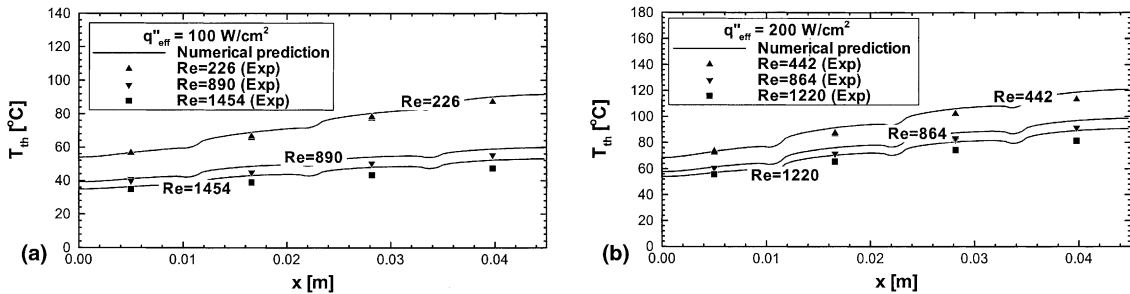

Fig. 7. Comparison of experimental data and numerical predictions for temperature distribution along thermocouple line: (a) $q''_{eff} = 100$ W/cm^2, (b) $q''_{eff} = 200$ W/cm^2.

proves the conventional Navier–Stokes and energy equations can adequately predict the pressure drop and heat transfer characteristics of the micro-channel heat sink. Based on the present results as well as those reported in several recent studies (e.g., [17,19]), it is expected that fluid flow and heat transfer within channels with characteristic dimensions greater than 100 µm and Reynolds numbers below 1700 should follow the conventional Navier–Stokes equations.

Having validated the numerical method, a more detailed depiction of the heat transfer characteristics of the heat sinks is now discussed.

3.3. Local and average heat transfer characteristics

The temperature distributions at several key planes of the unit cell are illustrated in Figs. 8(a)–(e) for $q''_{eff} = 100$ W/cm^2 and $Re = 890$. Note that the unit cell bottom wall (Wall A), channel bottom wall (Wall a), channel top wall (Wall c), and unit cell top wall (Wall C) are all x–y planes. Some interesting features are readily observed. The temperature increases along the longitudinal x-direction in all key planes except at the unit cell top wall (Wall C), where highest temperature is found about midway due to natural convection effects. In Fig. 8(a), the temperature distribution for the unit cell bottom wall (Wall A) shows shallow dips at the locations of

the deep slots. These dips are virtually eliminated when moving to the channel bottom wall (Wall a), Fig. 8(b), because of the excellent heat spread in the copper region between the two planes. There are very slight changes in the temperature gradient in the x-direction at the channel bottom wall (Wall a), Fig. 8(b), and channel top wall (Wall c), Fig. 8(c). In fact, a linear temperature rise can be regarded as a good approximation for both planes. The temperature along the transverse y-direction is virtually constant for all the x–y planes just discussed. As expected, the temperature decreases from the unit cell bottom wall to the unit cell top wall.

Notice that the channel side wall (Wall b) is an x–z plane. Fig. 8(e) shows higher temperatures for small z values close to the channel bottom wall (Wall a).

Figs. 9(a)–(c) illustrate the heat flux distribution along the channel walls for $q''_{eff} = 100$ W/cm^2 and $Re = 890$. The local heat flux, q'', is evaluated from

$$q'' = -k_s \frac{\partial T_s}{\partial n}\bigg|_\Gamma . \tag{24}$$

For all the channel walls, higher heat fluxes are encountered near the channel inlet. This is attributed to the thin thermal boundary layer in the developing region. The heat fluxes vary around the channel periphery, approaching zero in the corners where the flow is weak for
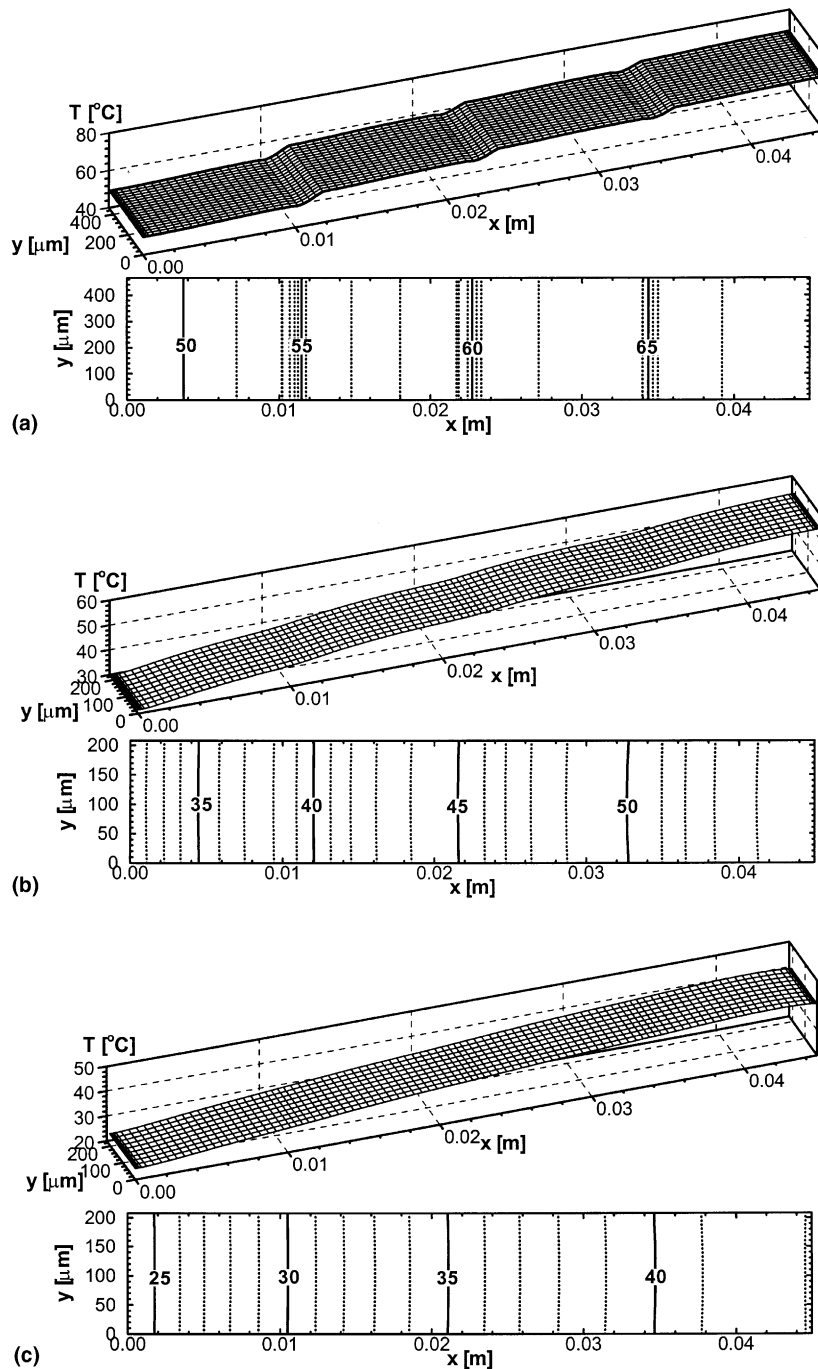
Fig. 8. Numerical predictions of local temperature distribution for $q''_{\text{eff}} = 100$ W/cm^2 and $Re = 890$: (a) unit cell bottom wall (Wall A), (b) channel bottom wall (Wall a), (c) channel top wall (Wall c), (d) unit cell top wall (Wall C), (e) channel side wall (Wall b).

a rectangular channel. The same conclusion concerning the vanishing heat flux in the corners is well documented in the heat transfer literature [24]. Fig. 9(b) shows heat transfer at the channel top wall (Wall c) is also very

weak. This is due to the very low thermal conductivity of the plastic cover plate (0.2 W/m °C) comparing with that of the copper block (401 W/m °C). Fig. 9(c) shows the heat flux along the channel side wall (Wall b) is higher
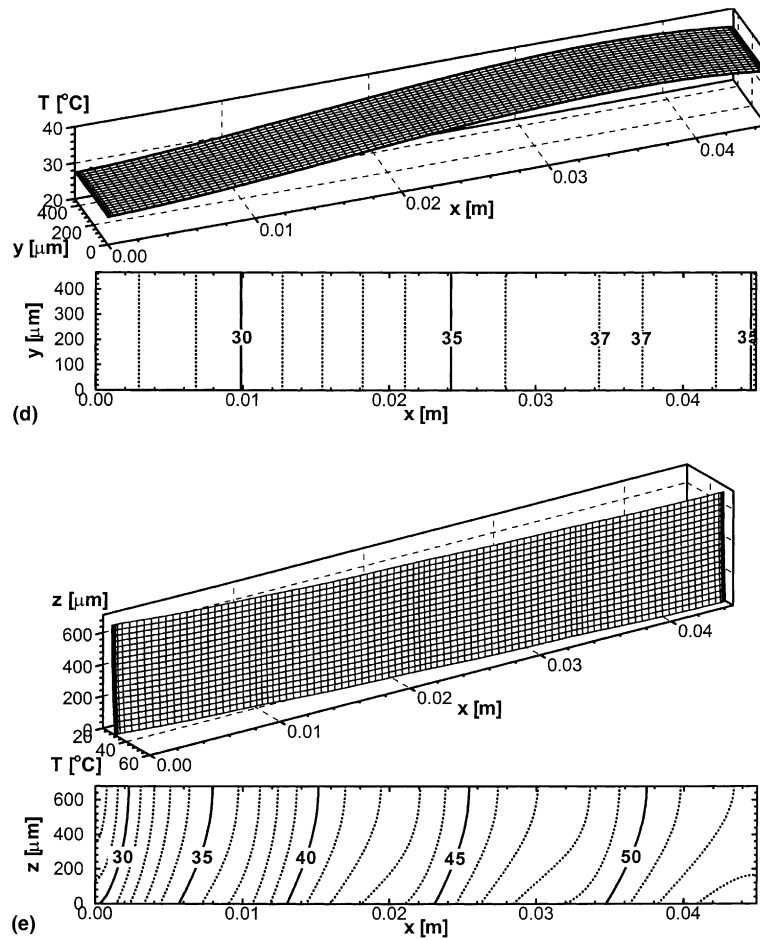
(d)

(e)

Fig. 8. (*continued*).

than along the channel bottom wall (Wall *a*) due to the short distance between the channel side walls and the large velocity gradient present.

The heat flux distribution can be better understood from the local Nusselt number distribution along the three channel walls, which is illustrated in Figs. 10(a)–(c). The local Nusselt number, *Nu*, is expressed as

$$Nu = \frac{q'' d_{\mathrm{h}}}{k_{\mathrm{f}}(T_{\mathrm{s},\Gamma} - T_{\mathrm{m}})}, \tag{25}$$

where T_{m} is the fluid bulk temperature defined as

$$T_{\mathrm{m}} = \frac{\int_{A_{\mathrm{c}}} uT \, \mathrm{d}A_{\mathrm{c}}}{\int_{A_{\mathrm{c}}} u \, \mathrm{d}A_{\mathrm{c}}}. \tag{26}$$

General features of the Nusselt number distribution are similar to those in the heat flux distribution, such as high value in the entrance region and low near the channel corners.

The fluid bulk temperature and average wall temperatures at the unit cell bottom wall (Wall *A*), channel bottom wall (Wall *a*), channel top wall (Wall *c*), unit cell top wall (Wall *C*), and thermocouple plane are plotted in Fig. 11(a) with respect to longitudinal distance *x* for $q''_{\mathrm{eff}} = 100$ W/cm^2 and $Re = 890$. The fluid bulk temperature T_{m} is given by Eq. (26), and the average wall temperatures at the unit cell bottom wall (Wall *A*), unit cell top wall (Wall *C*), and thermocouple plane are defined as

$$T_{\mathrm{av}}(x) = \frac{1}{W} \int_0^W T_{\mathrm{s},\Gamma} \, \mathrm{d}y \quad \text{for } z = 0, \ z = H \text{ and } z = H_{\mathrm{th}}. \tag{27}$$

The average wall temperatures at the channel bottom wall (Wall *a*) and channel top wall (Wall *c*) are defined as

$$T_{\mathrm{av}}(x) = \frac{1}{W_{\mathrm{ch}}} \int_{W_{\mathrm{w}}}^{W_{\mathrm{w}}+W_{\mathrm{ch}}} T_{\mathrm{s},\Gamma} \, \mathrm{d}y$$
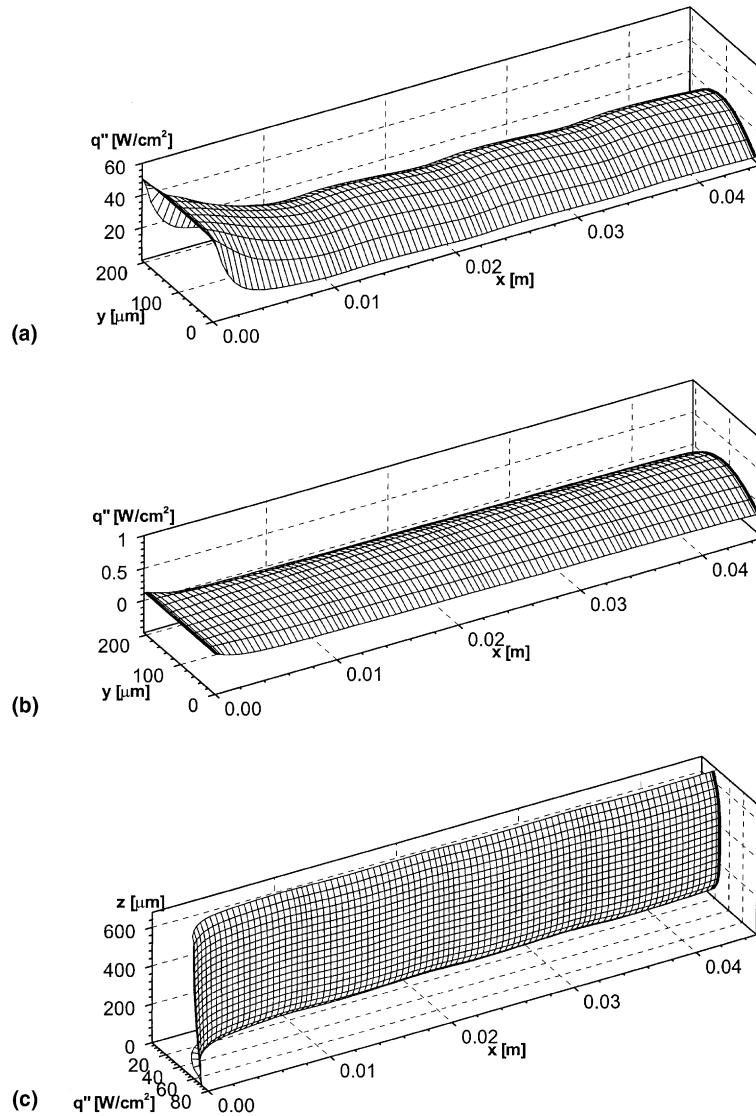$$\text{for } z = H_{\mathrm{w}2} \text{ and } z = H_{\mathrm{w}2} + H_{\mathrm{ch}}. \tag{28}$$

Fig. 9. Numerical predictions of local heat flux distribution for $q''_{\mathrm{eff}} = 100 \ \mathrm{W/cm^2}$ and $Re = 890$: (a) channel bottom wall (Wall a), (b) channel top wall (Wall c), (c) channel side wall (Wall b).

As expected, Fig. 11(a) shows the average temperature decreases from the unit cell bottom wall (Wall A) to the unit cell top wall (Wall C). The liquid bulk temperature is lower than all five solid wall planes. Slope changes of the water bulk temperature and average temperatures at the channel bottom wall (Wall a) and top wall (Wall c) are small, proving a linear temperature rise is a good approximation for these temperature distributions. The highest temperature point is located at the unit cell bottom wall (Wall A) immediately below the channel outlet.

Figs. 11(b) and (c) illustrate the average heat flux q''_{av} and average Nusselt number Nu_{av}, respectively, at the

channel bottom wall (Wall a), channel top wall (Wall c), and channel side wall (Wall b) for $q''_{\mathrm{eff}} = 100 \ \mathrm{W/cm^2}$ and $Re = 890$. The definitions of q''_{av} and Nu_{av} at the channel top wall (Wall a) and channel bottom wall (Wall c) are similar to that of the average wall temperature given in Eq. (28). q''_{av} and Nu_{av} at the channel side wall (Wall b) are defined, respectively, as

$$q''_{\mathrm{av}}(x) = \frac{1}{H_{\mathrm{ch}}} \int_{H_{\mathrm{w2}}}^{H_{\mathrm{w2}}+H_{\mathrm{ch}}} q'' \ \mathrm{d}z, \tag{29}$$

$$Nu_{\mathrm{av}}(x) = \frac{1}{H_{\mathrm{ch}}} \int_{H_{\mathrm{w2}}}^{H_{\mathrm{w2}}+H_{\mathrm{ch}}} Nu \ \mathrm{d}z \tag{30}$$
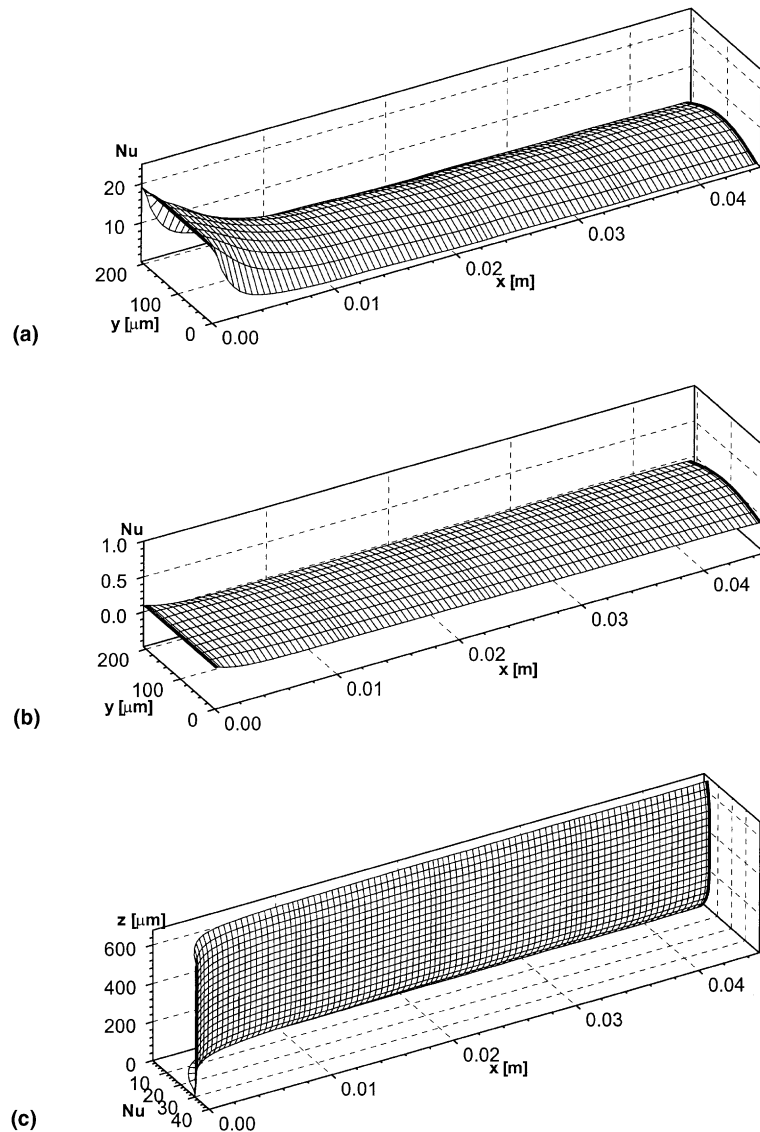
Fig. 10. Numerical predictions of local Nusselt number distribution for $q''_{\text{eff}} = 100$ W/cm^2 and $Re = 890$: (a) channel bottom wall (Wall a), (b) channel top wall (Wall c), (c) channel side wall (Wall b).

for $y = W_w$. Figs. 11(b) and (c) show the average heat flux and average Nusselt number are very small at the channel top wall (Wall c) compared to those at the other two walls. In fact, it is safe to assume the channel top wall (Wall c) is adiabatic. For the channel bottom wall (Wall a) and channel side wall (Wall b), the average heat flux and average Nusselt number are greatest near the channel inlet and decrease rapidly to nearly constant values. As indicated by Incropera and DeWitt [24], the hydrodynamic and thermal entry lengths of a circular tube may be estimated from

$$L_h = 0.05 Re\, d, \tag{31}$$

$$L_{\text{th}} = 0.05 Re\, Pr\, d, \tag{32}$$

respectively. For the rectangular channels of the present heat sink, the hydrodynamic and thermal entry lengths can be estimated by replacing the tube diameter d in Eqs. (31) and (32) with the hydraulic diameter, d_h. For the experimental conditions indicated in Fig. 11(c), the hydrodynamic and thermal entry lengths are 0.016 m and 0.081 m, respectively, assuming $Pr = 5.2$. From Fig. 11(c), it can be seen that flow is fairly well developed near channel exit, indicating Eq. (32) may not be accurate for rectangular channels. For most of the channel length, the average heat flux and average
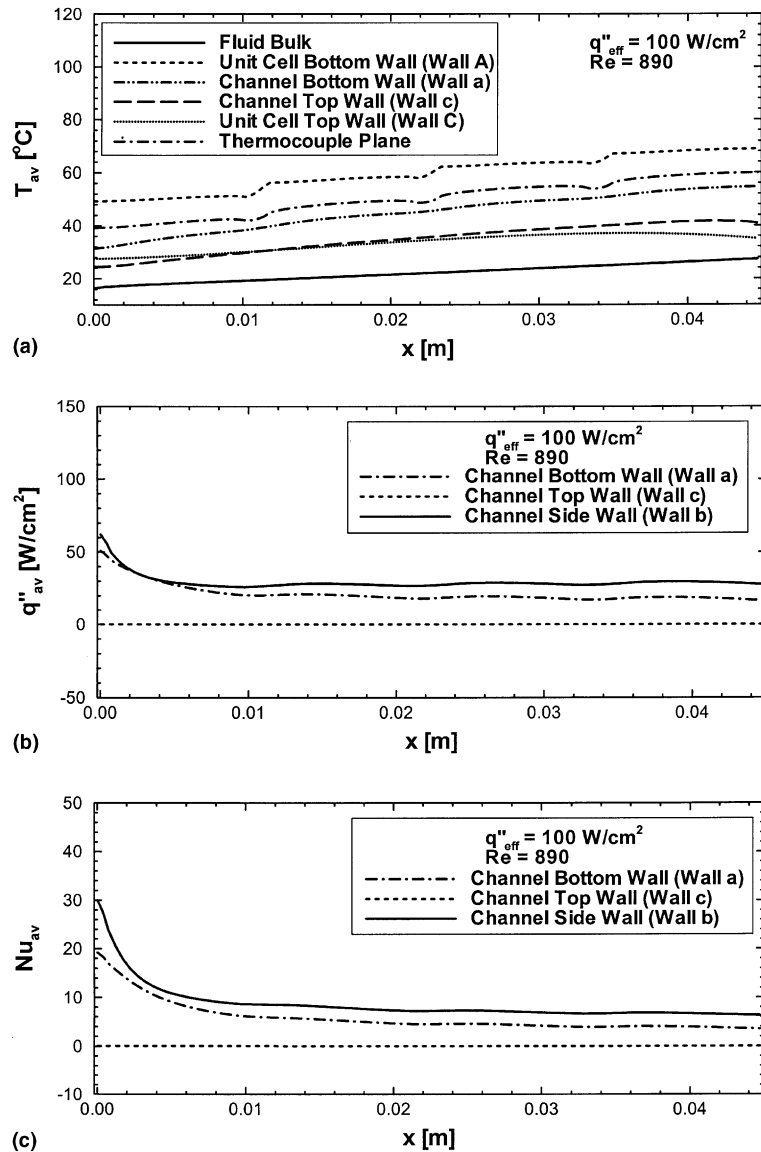
Fig. 11. Numerical predictions of average heat transfer characteristics for $q''_{eff} = 100$ W/cm^2 and $Re = 890$: (a) average temperature, (b) average heat flux, (c) average Nusselt number.

Nusselt number at the channel bottom wall (Wall *a*) are smaller than the corresponding values at the channel side wall (Wall *b*).

The theoretical values of Nusselt number for rectangular channels subjected to different thermal boundary conditions were summarized by Shah and London [25]. It would be ideal to compare the experimental results with either those theoretical Nusselt numbers or the present numerical predictions. Unfortunately, the present experiments alone cannot provide sufficient information to fully characterize the local and average Nusselt number or heat flux. During the tests, temper-

atures were measured at six points, which include the channel inlet and outlet as well as four locations inside the heat sink. Due to the limited temperature data and the complex nature of the conjugate heat transfer problem, the local and average *Nu* and *q''* cannot be determined without the numerical solution.

Figs. 12(a)–(c) show heat transfer characteristics for the conditions of $q''_{eff} = 200$ W/cm^2 and $Re = 864$. The average temperatures and average heat fluxes in Figs. 12(a) and (b), respectively, have the same trends as those presented in Figs. 11(a) and (b), but higher values. The average Nusselt number in Fig. 12(c) is
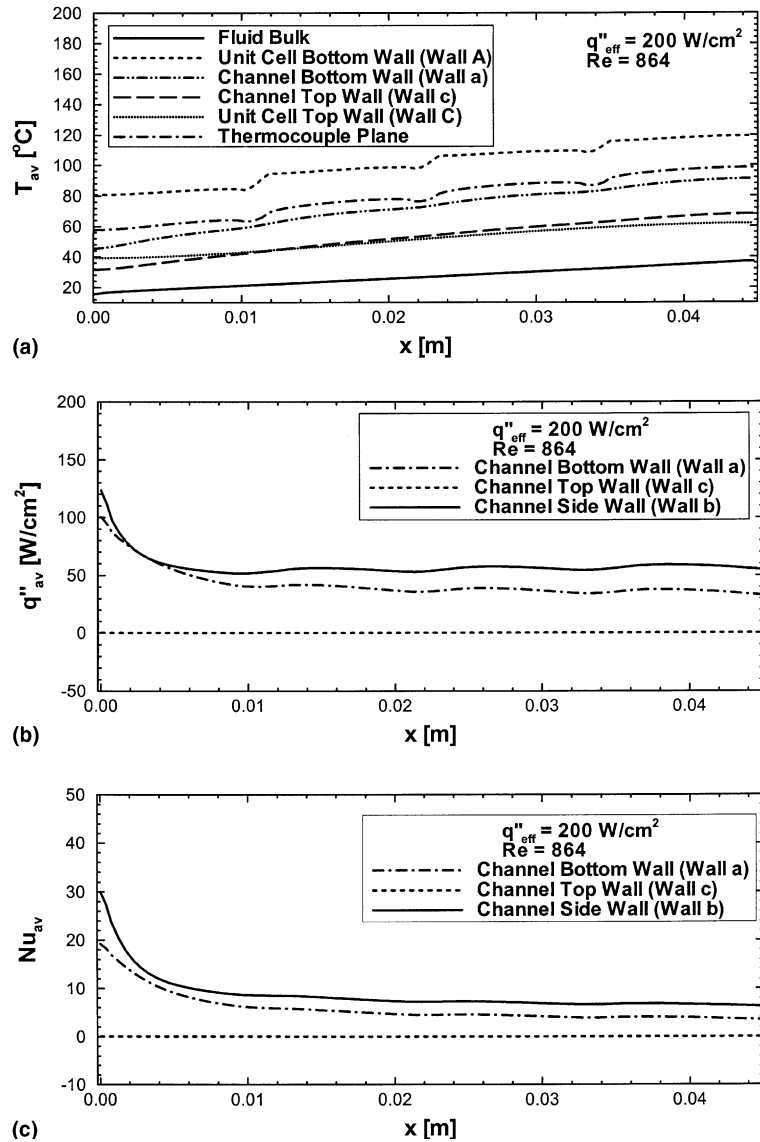
Fig. 12. Numerical predictions of average heat transfer characteristics for $q''_{eff} = 200$ W/cm^2 and $Re = 864$: (a) average temperature, (b) average heat flux, (c) average Nusselt number.

nearly identical to the one presented in Fig. 11(c). This is because the Nusselt number for laminar flow is determined solely by the channel geometry and the local flow conditions.

4. Conclusions

The fluid flow and heat transfer characteristics of a micro-channel heat sink were investigated both experimentally and numerically. Also presented and discussed was a detailed description of the local and average heat transfer characteristics of the heat sink, i.e. temperature, heat flux, and Nusselt number. Key findings from the study are as follows:

1. The measured pressure drop is in good agreement with the predicted values. A gradual slope change in the pressure drop variation with Reynolds number is attributed to the temperature dependence of water viscosity, and the increasing contraction and expansion pressure losses at the channel inlet and outlet, respectively, with increasing Reynolds number.
2. The early transition from laminar to turbulent flow cited in previous micro-channel studies was never observed in the present study within the tested Reynolds number range 139–1672.

3. Higher Reynolds numbers are beneficial at reducing both the water outlet temperature and the temperatures within the heat sink, alas at the expense of greater pressure drop.
4. Very good agreement was achieved between the experimental data and numerical predictions for the temperature distribution within the heat sink.
5. At any longitudinal distance x along the micro-channel, the bulk liquid constitutes the region of lowest temperature in the unit cell, while the highest temperature is encountered in the bottom wall (Wall A) immediately below the channel outlet. The water bulk temperature and average temperatures at the channel bottom wall (Wall a) and top wall (Wall c) increase fairly linearly along the longitudinal direction.
6. The channel top wall (Wall c) can be assumed adiabatic due to the small thermal conductivity of the plastic cover plate. For the channel bottom wall (Wall a) and side wall (Wall b), much higher heat flux and Nusselt number values are encountered near the channel inlet. The heat flux and Nusselt number also vary around the channel periphery, approaching zero near the corners.
7. Excellent agreement between both the pressure drop and heat sink temperature data and corresponding numerical predictions proves the conventional Navier–Stokes and energy equations can accurately predict the heat transfer characteristics of micro-channel heat sinks for the channel size employed in the present study and recommended for practical cooling applications.

Acknowledgements

References

[1] D.B. Tuckerman, R.F.W. Pease, High-performance heat sinking for VLSI, IEEE Electron. Dev. Lett. EDL-2 (1981) 126–129.
[2] R.W. Keyes, Heat transfer in forced convection through fins, IEEE Trans. Electron Dev. ED-31 (1984) 1218–1221.
[3] V.K. Samalam, Convective heat transfer in microchannels, J. Electron. Mater. 18 (1989) 611–617.
[4] R.J. Phillips, Micro-channel heat sinks, in: A. Bar-Cohen, A.D. Kraus (Eds.), Advances in Thermal Modeling of Electronic Components, vol. 2, ASME Press, New York, 1990, pp. 109–184.
[5] R.W. Knight, J.S. Goodling, D.J. Hall, Optimal thermal design of forced convection heat sinks – analytical, ASME J. Electron. Packaging 113 (1991) 313–321.
[6] R.W. Knight, D.J. Hall, J.S. Goodling, R.C. Jaeger, Heat sink optimization with application to microchannels, IEEE Trans. Components, Hybrids, Manufac. Technol. 15 (1992) 832–842.
[7] A. Bejan, A.M. Morega, Optimal arrays of pin fins and plate fins in laminar forced convection, ASME J. Heat Transfer 115 (1993) 75–81.
[8] D.Y. Lee, K. Vafai, Comparative analysis of jet impingement and microchannel cooling for high heat flux applications, Int. J. Heat Mass Transfer 42 (1999) 1555–1568.
[9] A. Weisberg, H.H. Bau, J.N. Zemel, Analysis of microchannels for integrated cooling, Int. J. Heat Mass Transfer 35 (1992) 2465–2474.
[10] A.G. Fedorov, R. Viskanta, Three-dimensional conjugate heat transfer in the microchannel heat sink for electronic packaging, Int. J. Heat Mass Transfer 43 (2000) 399–415.
[11] T. Kishimito, T. Ohsaki, VLSI packaging technique using liquid-cooled channels, IEEE Trans. Components, Hybrids, Manufac. Technol. CHMT-9 (1986) 328–335.
[12] S. Sasaki, T. Kishimito, Optimal structure for microgrooved cooling fin for high-power LSI devices, Electron. Lett. 22 (1986) 1332–1334.
[13] D. Nayak, L.T. Hwang, I. Turlik, A. Reisman, A high performance thermal module for computer packaging, J. Electron. Mater. 16 (1987) 357–364.
[14] M.M. Rahman, F. Gui, Experimental measurements of fluid flow and heat transfer in microchannel cooling passages in a chip substrate, Adv. Electron. Packaging ASME EEP-4 (1993) 495–506.
[15] M.M. Rahman, F. Gui, Design, fabrication, and testing of microchannel heat sinks for aircraft avionics cooling, in: Proceedings of the 28th Intersociety Energy Conversion Engineering Conference, vol. 1, 1993, pp. 1–6.
[16] T.S. Ravigururajan, J. Cuta, C.E. McDonald, M.K. Drost, Single-phase flow thermal performance characteristics of a parallel micro-channel heat exchanger, in: National Heat Transfer Conference, vol. 7, ASME HTD-329, 1996, pp. 157–166.
[17] T.M. Harms, M.J. Kazmierczak, F.M. Cerner, A. Holke, H.T. Henderson, J. Pilchowski, K. Baker, Experimental investigation of heat transfer and pressure drop through deep microchannels in a (1 0 0) silicon substarte, in: Proceedings of the ASME Heat Transfer Division, HTD-351, 1997, pp. 347–357.
[18] K. Kawano, K. Minakami, H. Iwasaki, M. Ishizuka, Micro channel heat exchanger for cooling electrical equipment, Appl. Heat Transfer Equip., Syst. Educ. ASME HTD-361-3/PID-3 (1998) 173–180.
[19] T.M. Harms, M.J. Kazmierczak, F.M. Cerner, Developing convective heat transfer in deep rectangular microchannels, Int. J. Heat Fluid Flow 20 (1999) 149–157.
[20] M.M. Rahman, Measurements of heat transfer in micro-channel heat sinks, Int. Commun. Heat Mass Transfer 27 (2000) 495–506.
[21] S.V. Patankar, Numerical Heat Transfer and Fluid Flow, Hemisphere, Washington, DC, 1980.
[22] S.V. Patankar, A numerical method for conduction in composite materials, flow in irregular geometries and conjugate heat transfer, in: Proceedings of 6th International Heat Transfer Conference, vol. 3, 1978, pp. 297–302.

[23] N.E. Todreas, M.S. Kazimi, Nuclear Systems I, Hemisphere, New York, 1990.

[24] F.P. Incropera, D.P. DeWitt, Fundamentals of Heat and Mass Transfer, fourth ed., Wiley, New York, 1996.

[25] R.K. Shah, A.L. London, Laminar Flow Forced Convection in Ducts: A Source Book for Compact Heat Exchanger Analytical Data, Suppl. 1, Academic press, New York, 1978.